Journal of Applied Physics ARTICLE scitation.org/journal/jap

Electric field induced migration of native point defects in Ga_2O_3 devices

Cite as: J. Appl. Phys. **133**, 035701 (2023); doi: 10.1063/5.0124543
Submitted: 27 October 2022 · Accepted: 28 December 2022 ·
Published Online: 17 January 2023

Micah S. Haseman,[1,a)] Daram N. Ramdin,[1] Wenshen Li,[2] Kazuki Nomoto,[2] Debdeep Jena,[2,3,4] Huili Grace Xing,[2,3,4] and Leonard J. Brillson[1,5]

AFFILIATIONS

[1]Department of Physics, The Ohio State University, Columbus, Ohio 43210, USA
[2]School of Electrical and Computer Engineering, Cornell University, Ithaca, New York 14853, USA
[3]Department of Materials Science and Engineering, Cornell University, Ithaca, New York 14853, USA
[4]Kavli Institute at Cornell for Nanoscale Science, Cornell University, Ithaca, New York 14853, USA
[5]Department of Electrical and Computer Engineering, The Ohio State University, Columbus, Ohio 43210, USA

[a)]**Author to whom correspondence should be addressed:** haseman.2@osu.edu

ABSTRACT

While the properties of β-Ga_2O_3 continue to be extensively studied for high-power applications, the effects of strong electric fields on the Ga_2O_3 microstructure and, in particular, the impact of electrically active native point defects have been relatively unexplored. We used cathodoluminescence point spectra and hyperspectral imaging to explore possible nanoscale movements of electrically charged defects in Ga_2O_3 vertical trench power diodes and observed the spatial rearrangement of optically active defects under strong reverse bias. These observations suggest an unequal migration of donor-related defects in β-Ga_2O_3 due to the applied electric field. The atomic rearrangement and possible local doping changes under extreme electric fields in β-Ga_2O_3 demonstrate the potential impact of nanoscale device geometry in other high-power semiconductor devices.

INTRODUCTION

The ultrawide bandgap semiconductor β-Ga_2O_3 has a very high predicted critical breakdown electric field ($E_{br} \sim 8$ MV/cm), making it very promising for high-power electronics.[1–5] In power devices, electric fields concentrated at electrode edges often result in permanent failure before reaching a uniform distribution of the intrinsic E_{br} within the device, thus limiting the ability to reach the maximum expected V_{br}. The field engineering challenges are exacerbated in Ga_2O_3 since the material system does not afford a high-quality p–n junction capable of avalanche yet. However, breakdown voltages for vertical device architectures can be substantially improved by integrating a dielectric fin/trench structure at the metal anode–semiconductor interface.[6–11] In vertical trench Schottky barrier diodes (SBDs), a reduced surface electric field (RESURF) reduces the leakage current, thereby enabling higher V_{br} as demonstrated by our group.[7,11,12] With continued improvements in device design to apply even stronger electric fields, the microscale changes in such highly non-equilibrium environments become even more important to understand. In particular, strong electric fields together with high thermal load are expected to move intrinsic electrically active point defects, resulting in atomic scale rearrangement within high-power device structures in general. Here, we investigate the effects of electrical stressing on β-Ga_2O_3 vertical trench Schottky barrier diodes by spatially resolved cathodoluminescence (CL) spectroscopy. The changes in CL before and after bias suggest that the electric field most likely induces the migration of point defects, specifically donor species that move below trench corners. These results demonstrate the need to consider defect electromigration in β-Ga_2O_3 device design for operation in extreme environments.

EXPERIMENTAL

Figure 1 outlines the experimental sequence beginning with Ga_2O_3 vertical device fabrication, which first involves etching a fin/trench pattern in the hydride vapor phase epitaxy (HVPE) overlayer followed by the deposition of an insulating 100 nm Al_2O_3

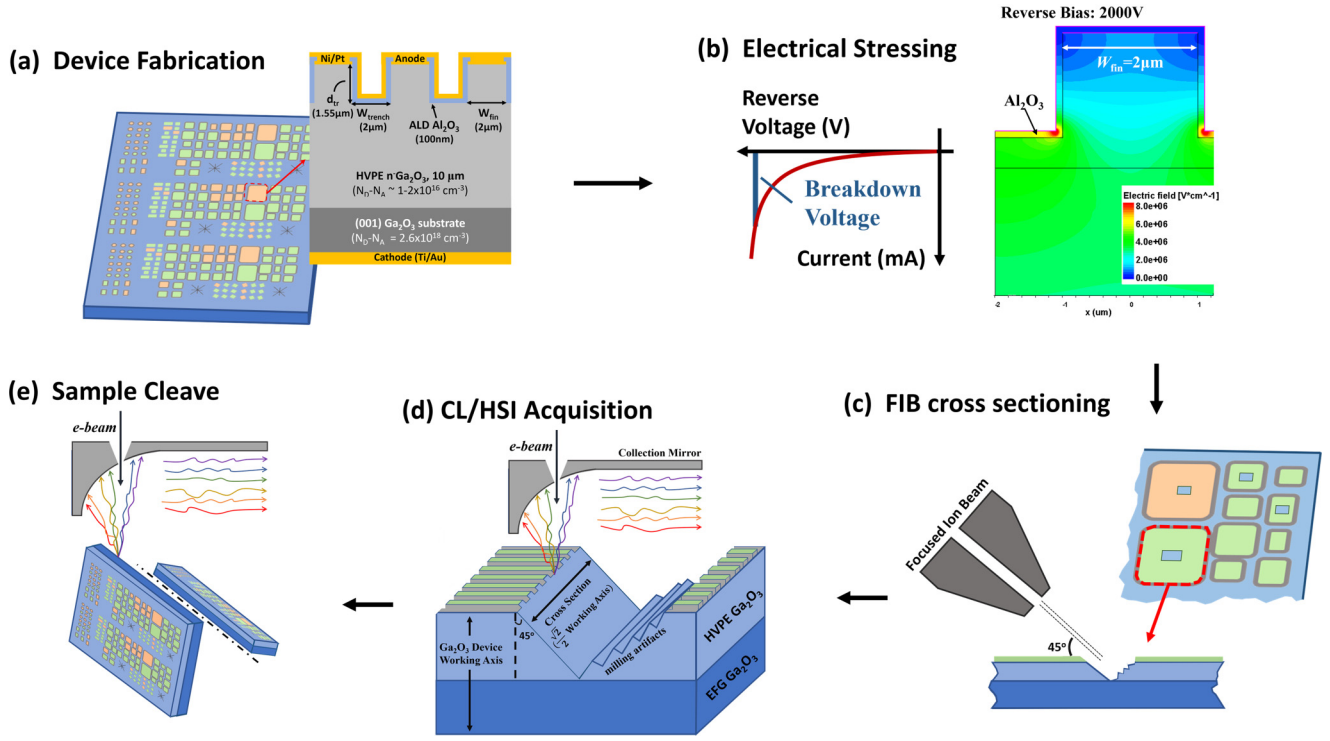

FIG. 1. Experimental sequence. (a) Representative schematic of the device array and the vertical geometry in cross section. (b) Schematic showing electrical stressing carried out under reverse bias with simulated electric field distribution. The RESURF effect shifts the maximum electric field away from the anode–semiconductor interface. Imaging of broken devices reveals that the visible damages, i.e., craters of materials as a result of destructive breakdown, occur along the device periphery due to unoptimized edge field management, while no morphology changes are observed in the device center. (c) Focused ion beam (FIB) milling schematic. Cross sections of electrically stressed and as-grown devices were exposed by Ga ion milling 45° relative to surface normal. All the exposed device cross sections subject to cathodoluminescence (CL) in this study are taken far away from the device peripheries to minimize the impact of dramatic mass transport associated with the highly localized destructive breakdown of the device. (d) Cathodoluminescence (CL) acquisition setup showing Ga_2O_3 vertical SBD angled cross section with parabolic collection mirror in position. (e) HVPE/EFG stack cleave and CL acquisition geometry.

layer via atomic layer deposition (ALD) and patterning to coat the base and sidewalls of the trenches, forming the dielectric layer. A Ni/Pt layer forms the top (anode) contact, and an ohmic Ti/Au back contact forms the cathode. Detailed sample growth and device fabrication details can be found in Li *et al.*[7] Figure 1(a) presents the schematic of the vertical Schottky barrier diode (SBD) array and representative cross section geometry. This design enables a RESURF effect, which modifies the electric field distribution, reducing the electric field strength at the metal–Ga_2O_3 interface, thereby increasing V_{br} under reverse bias as shown by the simulated electric field distribution in Fig. 1(b). All devices tested in this study first underwent forward bias from 0 to 3–5 V to verify the expected Schottky barrier turn-on. Subsequently, electrically stressed devices were subjected to quasi-static reverse current–voltage measurements from 0 V to breakdown ($V_{br} \approx -2$ kV) with a typical measurement time of approximately tens of seconds. Devices not subjected to breakdown voltages were tested under reverse bias from 0 to −50 V. We refer to these devices as "unstressed" given the nearly 2 orders of magnitude smaller applied field relative to stressed devices. Moreover, under the moderate bias conditions (−50 to +3–5 V), we have confirmed that charge trapping near the metal–insulator–Ga_2O_3 interface in these vertical trench power diodes is negligible.[13]

After stressing, device cross sections were exposed by 30 keV focused Ga ion beam milling at 45° relative to the sample surface as shown in Fig. 1(c). This geometry enables cathodoluminescence (CL) imaging of a 45° angled cross section, effectively along the device's working axis when viewed from above, perpendicular to the sample surface, with a parabolic collection mirror in position. This is shown schematically in Fig. 1(d). Imaging of failed devices reveals that the visible damages, i.e., craters of materials as a result of destructive breakdown, occur along the device periphery due to unoptimized edge field management, while no morphology changes are observed in the device center. Thus, all the exposed device cross sections subject to CL in this study are taken away from the device peripheries to minimize the impact of dramatic mass transport associated with the highly localized destructive breakdown of the device (SEM images can be found in the supplementary material). The CL penetration depth for $E_b = 10$ keV is approximately 200 nm, which extends well past the ion beam

implantation depth of 30 nm for the 30 keV Ga ion beam used in device cross sectioning (Fig. S1 in the supplementary material). Thus, any potential surface damage induced by the milling should have a minimal impact on the CL spectra. The CL spectra were acquired in a JEOL 7800F ultrahigh vacuum (UHV) scanning electron microscope (SEM) equipped with an aluminum parabolic mirror and connected to an optical train consisting of a Czerny–Turner configured spectrometer with an Andor air-cooled charge coupled device (CCD). Hyperspectral images (HSIs) were generated by modulating the scan rate and dwell time of the SEM electron beam to create a pixelated grid, wherein each pixel contains an entire CL spectrum. This allows CL peak amplitude maps to be generated that are normalized by the total CL intensity at each pixel, removing potential ambiguities that could arise from differences in optical path length along the sloped cross section. A second normalization was carried out with respect to the inherent emission of the edge-defined film-fed growth (EFG) substrate. The sample was cleaved to expose a clean HVPE epilayer and EFG substrate cross section without ion milling artifacts and without the influence of electrical stressing as shown in Fig. 1(e). CL spectra obtained from the substrate portion of this cleaved cross section were used as the second, global normalization reference. In other words, the intensity maps show the UV peak intensities relative to the untouched EFG substrate, where values >(<) 1.00 signify intensities greater than (red) vs less than (blue) corresponding substrate intensities.

RESULTS

Figure 2(a) shows the representative CL spectrum for the Ga_2O_3 devices measured. The spectra can be deconvolved into four Gaussian distributions centered at 2.85, 3.2, and 3.6 eV with a shoulder at 3.9 eV. Artifacts from the diffraction grating second order peak replicas generate the emission between 1.6 and 1.9 eV. The dominant CL peaks are in the ultraviolet (UV) at 3.2 and 3.6 eV. Hyperspectral images of the UV emission for the cross section of an SBD after electrical stressing are shown in Figs. 2(b) and 2(c). Hyperspectral images for a similar, unstressed device are shown in Figs. 2(d) and 2(e). Each CL spectrum in the HSI 3D array is first normalized by its integrated total CL intensity to account for absolute peak intensity variations and then renormalized by a global reference obtained from the respective UV emissions of the EFG substrate. Figures 2(b) and 2(c) show the clear redistributions of the dominant 3.2 and 3.6 eV UV peak intensities in the lower portion of the device HVPE epilayer, within a micrometer below the trenches, with only minor variations in the fin

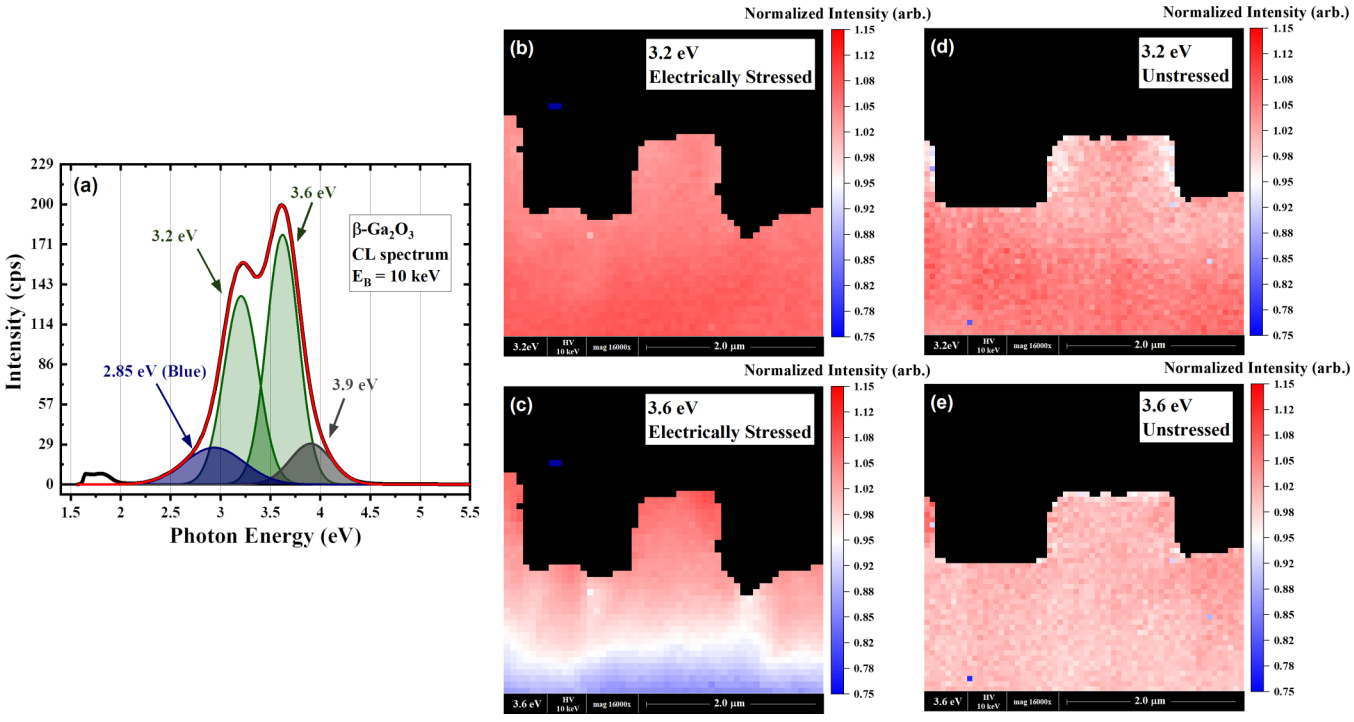

FIG. 2. (a) Representative CL spectra of Ga_2O_3 vertical SBD deconvolved with four Gaussian peaks at 2.85, 3.2, 3.6, and 3.9 eV. (b) and (c) Hyperspectral images (HSIs) of an electrically stressed Ga_2O_3 vertical device showing relative redistributions of 3.2 and 3.6 eV features. Highly segregated 3.6 vs 3.2 eV CL defect intensities are evident near the trench corners with pronounced gradients extending 1 μm below, while the fins exhibit only minor variation. (d) and (e) HSI of an unstressed device showing uniform peak distributions before electrical stressing. Since the bandgap emission for Ga_2O_3 was not observable, the spectra are normalized with respect to each spectrum's total integrated CL intensity and then normalized by the intensity of the respective UV emissions of the EFG substrate. The larger fin width for the unstressed device is due to different device geometries.

region. This is in contrast to the UV distributions for the unstressed device in Figs. 2(d) and 2(e) showing uniform peak distribution prior to high biasing, indicating that redistributions are unique to trench diodes that have been subjected to electrical stressing. Indeed, we find vertical peak redistribution, parallel to the applied field, in all electrically stressed devices measured, occurring predominantly below device trenches as shown in Fig. S2 in the supplementary material. The specifics of the fin/trench geometries and proximity to macroscale device failure influence the exact nature of peak redistribution. The HSI maps in Figs. 2(b) and 2(c) represent a dramatic example of UV peak redistribution and demonstrate the influence of the fin/trench geometry on the electric field distribution within the vertical devices that leads to a RESURF effect where the maximum electric field at the metal (anode)–semiconductor interface decreases[14,15] and shifts down the working axis toward the trench corners and below, while the electric field in the fins is significantly reduced as shown in Fig. 1(b). Indeed, the UV peak redistributions in Figs. 2(b) and 2(c) occur throughout the HVPE cross section from the Ni/Ga_2O_3 interface and into the bulk, with the most pronounced redistribution primarily below the trench corners rather than the top of the fins. As will be shown in the point spectra from within the diodes, the extracted spectra in the fin region are nearly uniform, while the spectra extracted from below the trench corners have appreciable UV peak redistribution. Magnified HSI maps of the fin region for a similar device (Fig. S3 in the supplementary material) show nearly uniform CL peak distributions above the trench after electrical stressing.

Figure 3 plots the HSI maps for the Ga_2O_3 stack (the HVPE epilayer on the EFG bulk substrate) cross section exposed by sample cleaving rather than the focused ion beam. Not only do these plots eliminate potential ion milling induced artifacts, they allow for the direct comparison of HVPE vs EFG grown Ga_2O_3. The normalized UV peak distributions in Figs. 3(a) and 3(b) show that the 3.2 eV emission is uniformly distributed in both the epilayer and bulk, while the 3.6 eV peak is slightly more pronounced in the HVPE epilayer. A stronger contrast is evident in Fig. 3(c), showing an increased total CL intensity in the HVPE epilayer relative to the EFG substrate and may be indicative of improved crystallinity in the HVPE layer, as discussed further below.

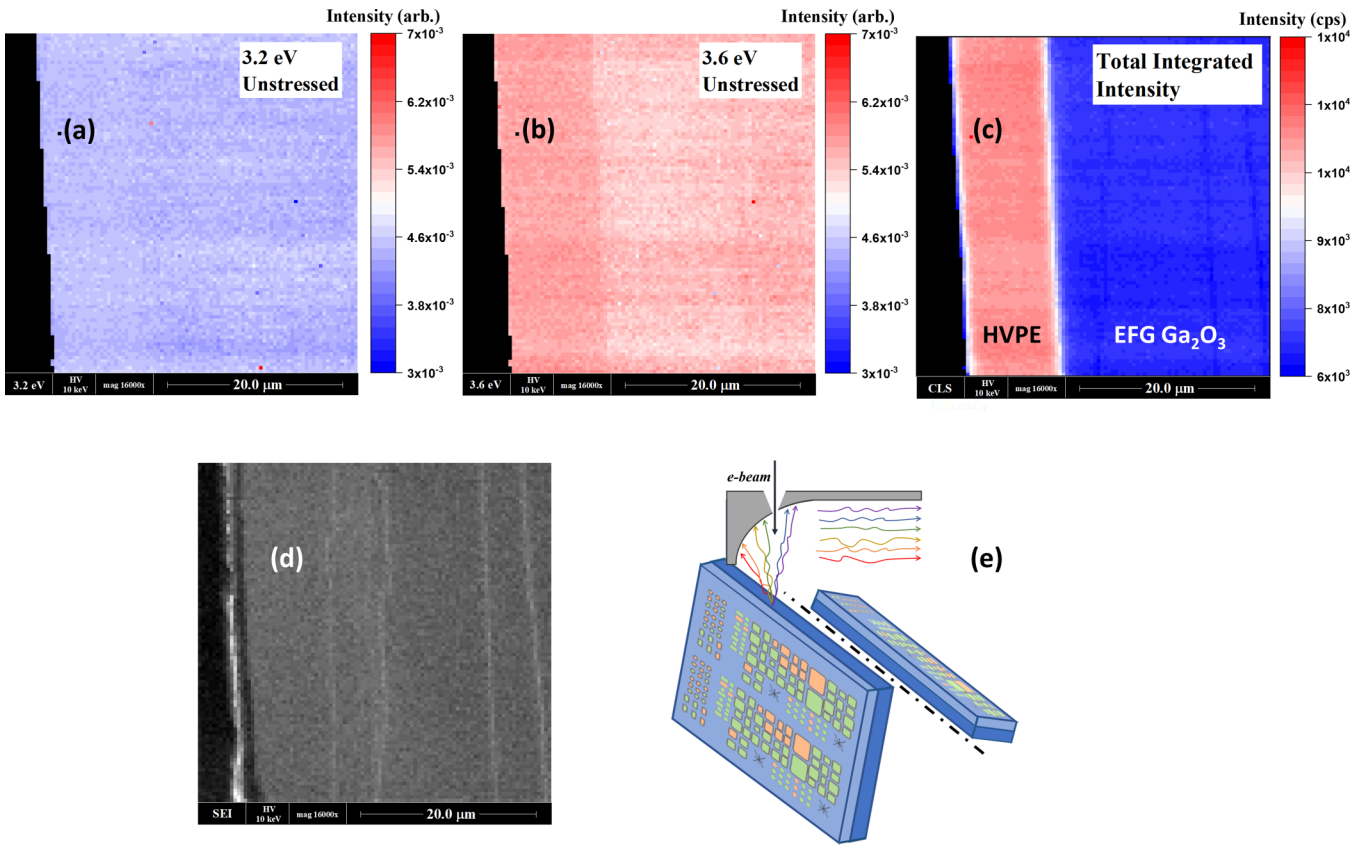

FIG. 3. Hyperspectral images of cleaved Ga_2O_3 stack with the HVPE epilayer on the EFG bulk substrate for the 3.2 (a) and 3.6 eV (b) peak distributions. (c) Hyperspectral image of cross section for total integrated CL intensity. (d) Secondary electron image. (e) Schematic of cleaved cross section and measurement setup. The HVPE epilayer and the EFG substrate have uniform UV distributions prior to biasing.

Since the high field during reverse bias introduces excess band bending and increases current flow in the HVPE region, the contributions from Joule heating in Fig. 2's HSI are likely significant. The applied field and elevated current increase electron–phonon scattering, increasing the temperature locally. This effect is more pronounced in Ga_2O_3 due to its poor thermal conductivity and inefficient heat dissipation compared with other high-power semiconductors. As described in the Experimental section, the apparent device morphology changes result from current filament formation during destructive breakdown and occur at one or a few spots along the device periphery, while most of the active device region away from these spots appears to show no morphology changes where the cross-sectional CL studies were taken. Nonetheless, the device regions studied by CL underwent a thermal shock during breakdown. Since Ni/Ga_2O_3 Schottky devices reportedly fail when annealed above 350°C,[16,17] we carried out 400 °C rapid thermal annealing under Ar flow for 5 min to best approximate a limiting case for the thermal environment induced by the reverse biasing. To minimize the effects of carrier gas choice and edge diffusion, the sample was annealed first and then subsequently cleaved to reveal the HVPE/EFG interface far from any exposed edges. The cross-sectional HSIs for the annealed sample are shown in Figs. 4(a)–4(c). The variation in the total CL intensity in Fig. 4(c) is likely a result of imperfect cleaving and variation in the sample–mirror distance as both the HVPE and EFG layers exhibit the same increase in the intensity from bottom-left to top-right. Point spectra in Fig. 4(d) compare the annealed and as-grown samples, while point spectra in Fig. 4(e) compare the electrically stressed and as-grown samples. The annealed sample has a marked decrease in 3.6 eV intensity [Fig. 4(d)] similar to the spectra for the electrically stressed device taken below the trenches [spot 30 in Fig. 4(e)]. However, the HSI in Figs. 4(a) and 4(b) shows that both 3.6 and 3.2 eV peaks are uniformly distributed in the annealed sample with no trends toward the Ni/Ga_2O_3 interface. Likewise, the behavior of the 3.2 eV peak is distinct from the stressed device and exhibits a relatively uniform distribution before and after annealing that contrasts the increased 3.2 eV peak intensity in the electrically stressed device extending away from the Ni/Ga_2O_3 interface and into the bulk. Additionally, the blue emission between 2.5 and 3.0 eV is significantly more pronounced in the annealed case vs electrically stressed case and displays an apparent red shift that is absent in the stressed device. While the CL spectra and HSI in Fig. 4 suggest that

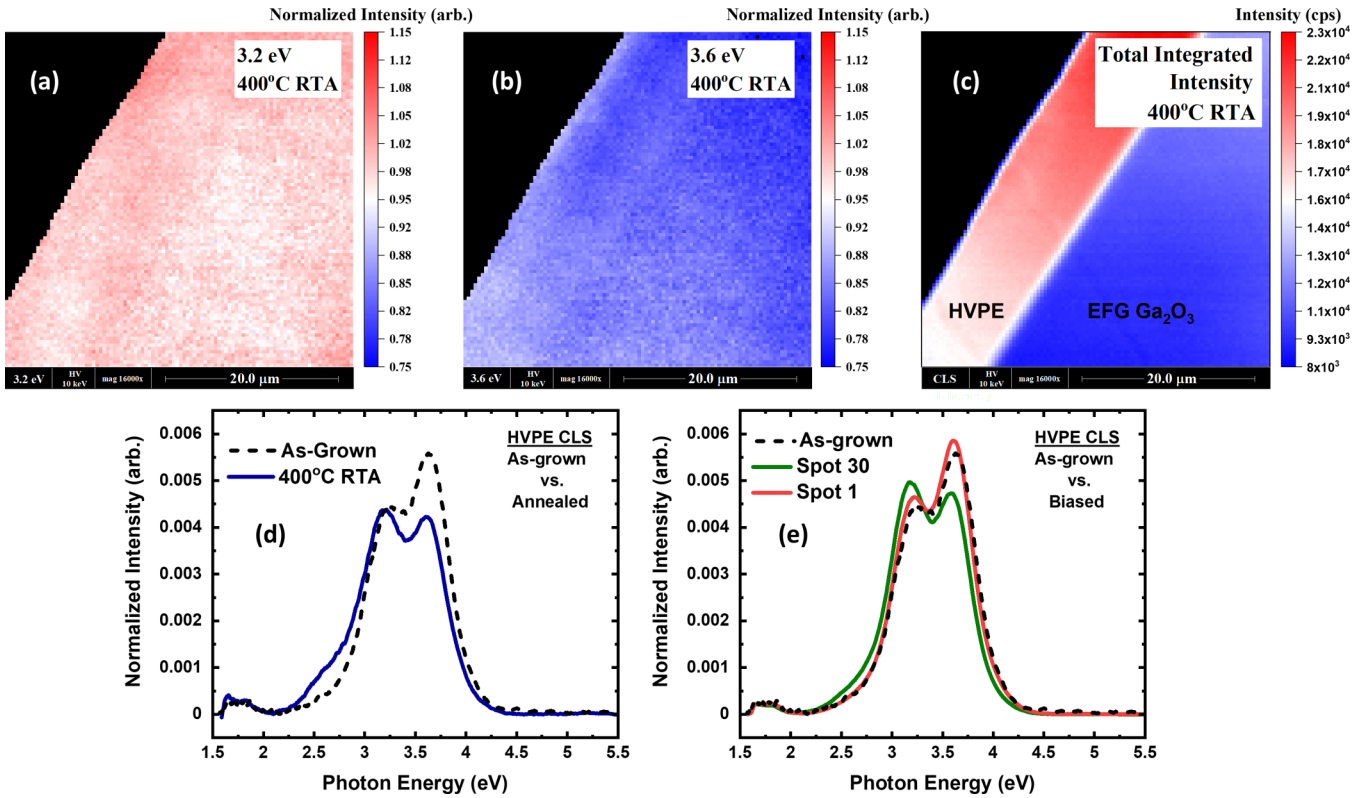

FIG. 4. CL hyperspectral images (HSIs) and point spectra of the rapid thermal annealed sample at 400 °C in Ar for 5 min. (a) 3.2 and (b) 3.6 eV HSI maps showing uniform distribution after annealing. (c) Total CL intensity map. The intensity gradient from bottom-left to top-right is an artifact of the cleaving process. (d) Point spectra of the as-grown sample vs annealed sample. (e) Point spectra of the electrically stressed sample vs as grown. Spot 1 is taken at the top of the device, near the Ni/Ga_2O_3 interface, and spot 30 is taken approximately 2 μm below the trench corner.

some contribution from thermal effects during reverse biasing are present, they cannot completely account for what are likely the electric field-induced redistributions shown in Fig. 2.

DISCUSSION

To understand the electric field-driven CL peak distributions in Fig. 2, we must consider the possible origins of the UV emissions in Ga_2O_3, which have been attributed both to self-trapped excitonic (STE) recombination and to recombination involving native point defects. We discuss three interpretations for these emissions below.

The first interpretation is STE recombination, which in Ga_2O_3 arises from the O 2*p* nature of the valence band, a heavy hole effective mass, and small dispersion, leading to the formation of small Ga_2O_3 polarons. This results in both holes that are believed to become localized (self-trapped) on nearby oxygen atoms and self-trapped excitonic recombination with emission energies below E_g.[2,18–21] Moreover, due to the low symmetry monoclinic crystal structure, holes localized at inequivalent lattice sites would split this energy band into distinct optical signatures. Accordingly, Fig. 5 defines the threefold coordinated oxygen sites as O_I ($2 \times Ga_{II}$, $1 \times Ga_I$) and O_{II} ($2 \times Ga_I$, $1 \times Ga_{II}$) and the fourfold coordinated site as O_{III} ($3 \times Ga_2$, $1 \times Ga_1$). Holes are theoretically predicted to stabilize at the threefold coordinated O_I and O_{II} sites giving rise to multiple UV peaks in the 3.2–3.6 eV range, where the lower energy peak is attributed to recombination involving a self-trapped hole (STH) at O_{II} and the higher energy peak to an STH at O_I.[19,22–24] Electron paramagnetic resonance (EPR) spectroscopy observations provide evidence for self-trapped holes via the angular dependence of the *g* matrix,[25] while polarization-dependent photoluminescence (PL)[26] and the convergence of PL Urbach tails[27] attribute UV emissions to STH_I and STH_{II}. Similar peak assignments have been carried out via temperature dependent CL with comparable peak splitting between 300 and 400 meV as shown here.[2,28,29]

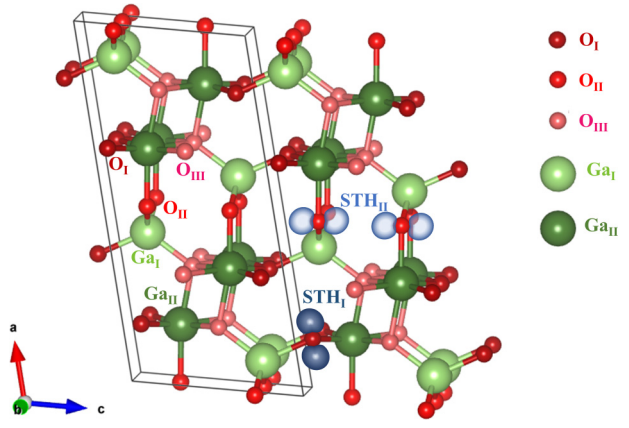

FIG. 5. The β-Ga_2O_3 crystal structure. The two inequivalent threefold coordinated oxygen sites are defined as O_I ($2 \times Ga_{II}$, $1 \times Ga_I$) and O_{II} ($2 \times Ga_I$, $1 \times Ga_{II}$). The fourfold coordinated site is O_{III} ($3 \times Ga_2$, $1 \times Ga_1$). Visual representations of potential self-trapped hole (STH) localizations are shown in blue, with STH_I occurring at an O_I site and STH_{II} between two adjacent O_{II} sites.

Since STHs are measured to be thermally unstable at room temperature,[25,28] holes generated by or present at the time of electrical stressing would have lifetimes too short to manifest in the post-operando CL spectra. Therefore, the holes involved in the STE recombination would need to be extrinsic in nature, generated by the incident electron beam during CL acquisition with subsequent hole localization. In order for the STE recombination to account for the redistribution of the UV emissions, it must be inherently linked to a species that is room temperature stable and that directly reflects the density of hole-localizing oxygen atoms. Thus, a likely mechanism for the changes in the UV emission is redistribution in local oxygen vacancy (V_O) concentrations (and thereby local oxygen atom configuration), which are electrically active and mobile under the applied reverse bias. Kyrtsos *et al.*[30] and Blanco *et al.*[31] have reported that the inequivalent lattice positions in Ga_2O_3 lead to unequal migration barriers for both cation and anion vacancies (V_{Ga} and V_O). Given the polarity of the electrical stressing under reverse bias, the positively charged V_O can be expected to migrate and accumulate near the trench corners in spatially different distributions. In this STE model, the UV emissions are not a direct manifestation of V_O—they are attributed to STH-related recombination. However, the changes in the UV emission are linked to the concentration and configuration of electrically active V_O and, thereby, the configuration of the remaining O_I vs O_{II} atoms. In general, Krytsos *et al.* calculate lower migration barriers for V_O^I vs V_O^{II} and V_O^{III} with the lowest barrier of 1.2 eV along the b-axis. These barriers could decrease by up to 0.2 eV in the presence of applied electric fields.[31] Based on the V_O^I's lower migration barrier, one could expect the preferential migration of V_O^I vs V_O^{II}, changing the relative 3.6 and 3.2 eV peak intensities. Indeed, Figs. 2(b) and 2(c) show a more pronounced 3.6 vs 3.2 eV peak redistribution. Oxygen vacancy accumulation might also reduce the overall STH peak emissions and account for the reduction in the CL intensity shown in Fig. S4 in the supplementary material.

The second UV peak interpretation and alternative consideration of the UV emissions directly involves theoretically predicted charge state transitions of the native point defects themselves at energies, which correspond closely to the approximate optical transition energies observed experimentally here and previously.[32,33] V_O is theoretically predicted to have three charge state transitions with energies ranging up to 3.5 eV,[34–36] close to the 3.6 eV emission shown here. Room temperature remote oxygen plasma treatments have provided evidence to correlate a ~3.5 eV UV emission with V_O from its systematic decrease in the normalized spectral intensity. Analogous experiments involving forming gas (FG) anneals and neutron irradiation have provided evidence for the hydrogen passivation of gallium vacancies in order to attribute a ~3.0 eV transition to V_{Ga}.[32,33] These assignments agree in principle with defect level energies measured via deep level transient spectroscopy and deep level optical spectroscopy (DLTS and DLOS, respectively) for trap state energies below the conduction band.[37,38] Indeed, the E_C −1.29 eV DLTS defect agrees well with the previous V_O assignment of ($E_G = 4.8$ eV) − 1.29 eV = 3.5 eV. Likewise, the E_C −2.0 eV DLTS trap state measurement agrees well with the previous V_{Ga} assignment of ($E_G = 4.8$ eV) − 2 eV = 2.8 eV, close to the 2.85 eV peak energy shown in Fig. 2(a). However, this emission is most

often attributed to V_O–V_{Ga} donor–acceptor pair (DAP) recombination.[24,39–45] Given the 0.4 eV disparity between the 3.2 eV feature and the DLTS associated E_c – 2.0 eV V_{Ga} defect level, the physical nature of the 3.2 eV peak appears distinct from the 3.0 eV V_{Ga} attributed peak reported previously.[32,33] Since emission in the 2.8–3.2 eV range is often attributed to V_O-related defects,[36,42,46] such an assignment for the 3.2 eV peak would explain the inverse behavior to the 3.6 eV peak where oxygen atom migration along one direction (increase in 3.6 eV toward trench) corresponds to an oxygen vacancy migration in the opposite direction (decrease in 3.2 eV toward trench). Nevertheless, given the association of oxygen vacancy filling by a remote oxygen plasma and FG passivation of a 2.85–3.0 eV peak, as well as the agreement between the 3.6 and 2.85 eV cathodoluminescence peak energies vs density functional theory (DFT) charge state transitions and DLTS/DLOS defect state energies, there is some evidence to suggest a possible native point defect related nature for the dominant optical emissions.

The blue emission should be considered within this point defect framework. Figure 6(a) displays the representative spectra along a vertical line cut in a stressed device and a slight increase in the "blue" 2.85 eV shoulder. This peak could be related to oxygen vacancy (V_O–R) sites via donor–acceptor pair (DAP) recombination, with V_{Ga} being the typical (deep) acceptor.[24,39–44] As V_O potentially accumulates near the trench corners, the 2.85 eV V_O–R peak intensity increases, although the effect is not as pronounced as the change in the 3.6 vs 3.2 eV emission. However, this is not unexpected as V_{Ga} have low migration barriers[30,31] and as acceptors would likely migrate away from the trench corners. Thus, the competing migration between the anion and cation vacancies could reduce the overall intensity of this emission. Furthermore, a decrease in V_{Ga}-related defects could further increase the local free carrier density since V_{Ga}-related deep levels are known compensating centers. The pronounced increase in blue luminescence that is observed with annealing shown in Fig. 4(d) is consistent with the literature reporting reduced N_D–N_A and increased V_{Ga} formation after annealing.[47,48] This suggests that even relatively low temperature RTA can generate additional point defects for short annealing times. However, a full elucidation of the thermal processing effects on Ga_2O_3 optical signatures is beyond the scope of this work. Likewise, further research is needed to fully elucidate the nature of V_{Ga}-related migration under strong electric fields.

The third interpretation for the UV peaks considers impurity species and point defect reconfiguration. Although the applied electric field under reverse bias may be sufficiently large to overcome the migration barriers of the native point defects, the contributions to the UV emission by potential impurity species either directly or indirectly by reconfiguration of the native defect species must also be considered. Moderate Si shallow donor doping has been shown to directly contribute to the UV emission in Ga_2O_3 via donor–acceptor pair (DAP) recombination; however, the doping density where this becomes relevant is above N_D–$N_A = 3 \times 10^{17}$ cm^{-3},[44] an order of magnitude higher than the doping density of the vertical devices here with N_D–$N_A \approx 2 \times 10^{16}$ cm^{-3}.[12] As such, DAP recombination by Si is not likely responsible for the UV emission. On the other hand, hydrogen species present during growth can incorporate in the lattice in various charge states both as interstitial and substitutional atoms and as passivating species, thus altering the configuration of the potentially UV emitting native defects. Moreover, the expected migration barrier for interstitial hydrogen

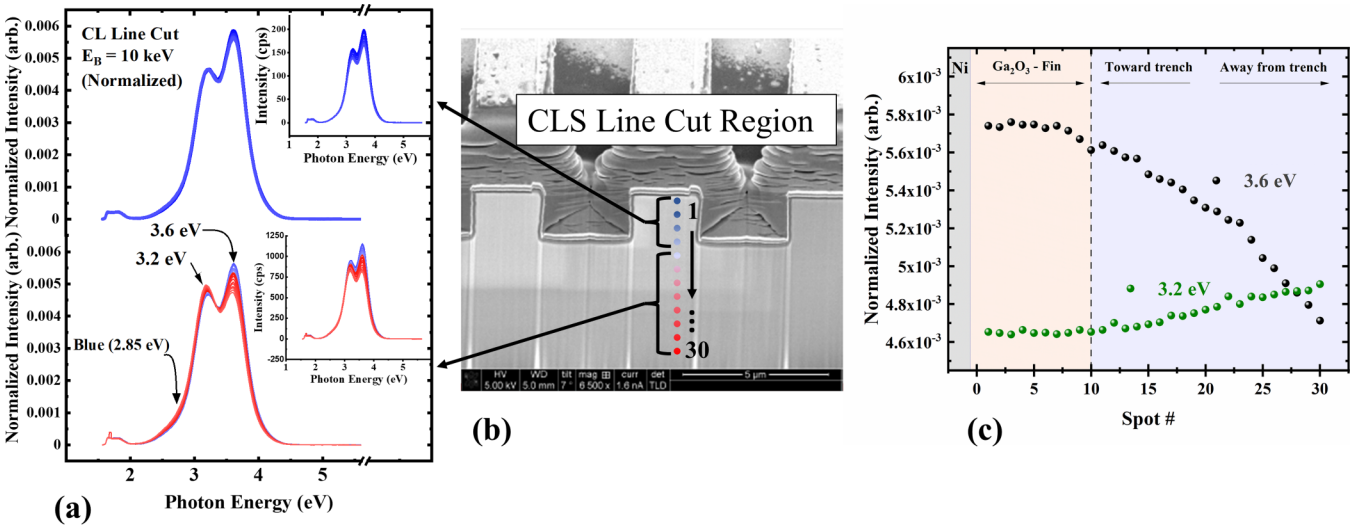

FIG. 6. Cathodoluminescence spectra along a vertical line cut of an electrically stressed Ga_2O_3 device. (a) CL spectra along a vertical line cut showing the uniform peak intensity in the fin region (top set of 10 spectra) and an increase in 3.6 vs 3.2 eV peaks approaching the trench corner from below (bottom set of 20 spectra). Normalization is with respect to each spectrum's total integrated CL intensity. The insets show the raw, unnormalized spectra. (b) SEI showing the location of the line cut. The slight horizontal changes in contrast are due to extended e-beam exposure. (c) Normalized 3.6 and 3.2 eV peak intensities plotted spatially along the line cut.

H_i^+ is quite small at 0.34 eV with the barrier for the dissociation of H_O^+ into H_i^+ and V_O^0 only 1.33 eV.[35,49] Thus, both species are expected to be mobile at moderate temperatures and under the applied electric field. Combined with the shallow donor nature of H_O^+ and H_i^+, hydrogen migration, diffusion, and accumulation in Ga_2O_3 devices can be significant. For example, such accumulation or depletion of donor species and corresponding changes in the local doping density would affect the device nature and operation.

Atomic hydrogen is amphoteric and can act exclusively as a donor impurity in some materials.[50] In Ga_2O_3, interstitial hydrogen is almost always a shallow donor and in the positive charge state H_i^+, with the ε (±) transition occurring just above the conduction band minimum (CBM).[35] This is relevant when considering the electromigration of preexisting hydrogen as the migration would predominately involve positively charged H_i^+ and H_O^+ rather than H^- (or neutral H). For the latter, the subsequent passivation of V_{Ga} is unlikely since migrating hydrogen would not be in the appropriate charge state for bonding with the nearby oxygen atoms. The formation of mobile H^- by the disassociation of preexisting V_{Ga}–H is also unlikely as these complexes are expected to be quite stable with large activation energies between 3.2 and 3.4 eV.[51] Indeed, the expected broad emission lines between 1.9 and 2.6 eV for V_{Ga}–H complexes[22,32] are not observed in any of the CL spectra used in the construction of the HSIs in Fig. 2. A more likely scenario is the migration of H_i^+ into preexistent V_O^0 forming H_O^+, effectively converting the V_O from a deep to shallow donor.[35,49,52] If the 3.6 eV emission is attributed to V_O, as postulated above, then the migration of H_i^+ into V_O would decrease the intensity of the associated 3.6 eV emission. This agrees well with the 3.6 eV peak distribution shown in Fig. 2(c) and corresponding reduction in the 3.6 eV emission intensity below the trench corners and the predicted electric field distribution shown in Fig. 1(b). However, just as the case with V_O, the migration of H_i is highly anisotropic, with the lowest barrier along [010],[49] in the direction of the vertical device fins and perpendicular to the biasing field, which is along [001]. As such, the barrier for H_i, but not necessarily H_O, is increased.

Table I summarizes the peak energies and origins from the three interpretations presented above. There are experimental and theoretical justifications for all of the proposed UV peak interpretations, and the broadness of the UV peaks makes possible the coexistence of several luminescence mechanisms. Indeed, the true nature of the UV emissions may involve a combination of STE and point defect related processes. However, given the increased total CL intensity for the HVPE epilayer vs EFG substrate shown in Fig. 3(c), it seems likely that these peak intensities correlate with overall sample crystallinity. The reported trap density for HVPE overlayers is 1–2 orders of magnitude lower than the bulk substrate,[53] translating to an increased crystallinity for the HVPE layer and, thus, improved self-trapping of holes by oxygen atoms. Typical metrics for assessing the HVPE epilayer quality like x-ray diffraction and electrical characterization show the comparable quality of the regrown HVPE epilayer to the host substrate.[54,55] Thus, the spectral intensity comparison by CL under identical acquisition parameters may be an advantageous characterization metric to supplement typical structural and electrical characterization techniques.

The CL taken along a vertical line cut in Fig. 6(a) shows two distinct UV peaks with a clear systematic variation along the device's working axis. The top set of spectra (spots 1–10) in Fig. 6(a) show nearly uniform UV distributions in the fin region, while the bottom set of spectra (spots 11–30) show a pronounced increase in 3.6 vs 3.2 eV approaching the trench corner from below. The approximate positions along the line cut are shown in Fig. 6(b). Although a gradient exists from the Ni/Ga_2O_3 interface and into the bulk as shown in Figs. 2(b) and 2(c), the majority of the spectral redistribution occurs between spots 11 and 30, which correspond to the termination of the trench corners and below. This is most apparent in Figs. 6(a) and 6(c), which show the 3.2 and 3.6 eV peak intensity variation from the Ni/Ga_2O_3 interface and into the bulk. Up to spot 10, the peak intensities are relatively constant. Between spots 11 and 30, the peak intensities diverge as the beam probes below the trench corner. Comparing the spectra of spots 1 and 30 with the as-grown sample, the 3.6 and 3.2 eV peaks exhibit a crossover. Near the Ni/Ga_2O_3 interface, the peak intensity is greater than that of the as-grown sample, dropping below when probing down the device's working axis, toward spot 30, as shown in Fig. 4(e). This shows that the peak redistribution is a defect migration effect rather than a gradient in defect creation/injection. Another important distinction is that the peak energies in the HSI are invariant and change only in their relative intensities. Since each device was subjected to a small forward test voltage, some injected electrons from the n-Ga_2O_3 layer might trap at the MIS interface,[11,13] which, under strong reverse bias, could detrap and redistribute. This would lead to a distribution in the charge

TABLE I. Summary of luminescence energies and underlying mechanisms discussed in peak interpretations.

STH	Si_{Ga}	V_O	V_{Ga}	V_{Ga}–V_O
3.2–3.6 eV (STH)[29]	3.2–3.6 eV[29]			2.8–3.0 eV[29]
3.4 eV (STH)[21]				
3.5 eV (STH_I), 3.1 eV (STH_{II})[56]				
3.3 eV (STH_I), 3.0 eV (STH_{II})[28,45]				2.8 eV[28,45]
		3.5 eV[32,33]	3.1 eV[32,33]	
		3.7 eV[57]	3.2 eV[57]	
			2.7 eV[39]	3.0 eV[39]

state configurations and, hence, optical emission energies of nearby point defects. However, we observe no variation in optical transition energies that would arise from a variation in the point defect charge state.

It is important to note that, regardless of the specific spectral assignment, all of the above UV peak interpretations indicate an electrical field-driven redistribution of either intrinsic or extrinsic point defects. This is significant because the rearrangement of charged defect species after or during biasing could lead to changes in local doping density. In this case, the increase in defect-/donor-related emissions near the trenches shown in Figs. 2 and 6 would increase the Ga_2O_3 effective doping in this region, either by oxygen vacancy or vacancy-cluster accumulation that enables hopping between donor clusters,[56,58] or by the accumulation of shallow donors H_i^+ and H_O^+, with the latter converting deep donor V_O to shallow donors. The normalized 3.6 eV peak intensity in Fig. 6(c) changes from .0047 to .0056, increasing by a factor of 1.2×. This could mean an increase in the effective carrier density (N_D) by up to 1.2×, and a decrease in the depletion width (W) by up to $1/\sqrt{1.2x}$ for the same voltage drop in Ga_2O_3 since W is inversely proportional to $\sqrt{N_D}$. With the narrowing of the depletion region, the electric field would fall across a narrower combined dielectric separation, i.e., across the combined Al_2O_3 insulator plus thinner Ga_2O_3 depletion region thickness. This is shown schematically in Fig. S5 in the supplementary material. In terms of device dielectric breakdown, the total insulator plus Ga_2O_3 depletion width would decrease with this donor accumulation, increasing the electric field proportionally at the trench corners where the field is already maximized via the RESURF effect.[12,59] Alternatively, as the vertical device undergoes breakdown, excess heat generated by the high currents could induce the UV peak redistributions via defect diffusion during thermal runaway. Indeed, the decrease in the 3.6 eV peak observed for the rapid thermal annealed sample is similar to the same peak decrease observed for the reverse biased device. Interestingly, since the electrical stressing was carried out quickly, on the order of a few tens of seconds, this would suggest that any breakdown-induced defect redistribution happens very abruptly. The possibility that defect redistribution occurs *in-operando* underscores the importance of field-induced defect migration. However, to fully elucidate this causality, future studies to obtain *in situ* luminescence spectra would be needed while simultaneously biasing to understand whether defect peaks redistribute leading up to breakdown or upon device failure. The geometry constraints involving FIB processing limit simultaneous biasing and CL acquisition for this work's devices. Future studies using simpler device geometries that allow for *in situ* CL acquisition while applying large reverse bias are currently underway.

The electric field-induced migration of point defects presents an interesting challenge for Ga_2O_3 devices, and it may be necessary to target the removal of kinetic donor species prior to device fabrication and processing. In wide bandgap oxides, it is possible to form a defect-rich layer via thermal processing driven by impurity migration toward the sample surface, wherein the sacrificial layer is removed by chemical or mechanical polishing.[60] This would enable bulk sample processing to remove mobile donors prior to individual device fabrication, effectively treating many devices simultaneously. Hydrogen impurities present a more difficult problem to address. It has been shown that H can be driven out under UHV conditions,[61] reducing the reservoir of potential donor species, but the challenge remains of limiting the reabsorption of H during subsequent handling outside vacuum and extreme care would be needed to process materials into devices without excess H exposure. The removal of hydrogen, if possible, would also minimize the impact of V_O-related defects by inhibiting the reconfiguration of V_O from a deep to shallow donor via the migration of H_i or V_O. Alternatively, rather than donor removal, one could increase the local density of compensating species, for example, by implanting acceptor ions[62] at targeted depths where the electric field is expected to be high, and the impact of donor species is expected to be large. For the devices here, compensating impurities implanted in the HVPE layer ~1 μm below the surface, prior to device fabrication, could locally compensate the elevated donor concentrations resulting from the electric field-induced migration. But perhaps a convenient solution is to simply take advantage of Ga_2O_3's low crystal symmetry. Since the migration barriers of V_O and H_i are highly anisotropic, a selective choice of the contact geometry (and thus biasing direction) with respect to the crystal orientation can put the electric field along a direction where the migration of V_O and H_i are least favorable. In particular, the migration barriers are expected to be large along the [100] direction for both V_O and H_i, up to 2.6 and 2.95 eV, respectively.[49] Other considerations include the bandgap and, thus, critical field anisotropy in Ga_2O_3 as well as 3D field distribution in a fabricated device. Work by some of our authors has already demonstrated that the device geometry with respect to crystal orientation affects the interfacial state density[63] and thermal distribution during device operation.[64] The overall device design for reliability will need to take into account all the aforementioned discussions.

CONCLUSIONS

In summary, we used CL point spectra and HSI mapping to demonstrate how point defect related donor species in β-Ga_2O_3 vertical Schottky diodes migrate and redistribute upon high reverse electrical bias. The low crystal symmetry of the monoclinic crystal structure likely results in unequal migration energies for point defects on inequivalent lattice sites and along inequivalent crystallographic directions, suggesting a preferential migration of specific threefold coordinated oxygen vacancies and/or migration of positively charged hydrogen species, altering the relative intensity of the UV emissions that we observe via spatially resolved CL maps and linecuts. Together, the local electrical field maximum under reverse bias resulting from the fin/trench design and the potential for donor-related defect accumulation near SBD trench corners could lead to a local doping increase that would affect *in-operando* devices. More generally, defect migration and local doping changes under extreme electric fields in β-Ga_2O_3 demonstrate the potential impact of the nanoscale device geometry in other high-power semiconductor device structures. Several suggestions are made to curb the adverse impact of defect migration.

SUPPLEMENTARY MATERIAL

See the supplementary material for electron and ion beam implantation profiles, secondary electron and hyperspectral images

of vertical device cross sections, hyperspectral images of the fin region of the electrically stressed device, raw cathodoluminescence spectra along the line cut of the electrically stressed device, and band bending due to potential donor accumulation

ACKNOWLEDGMENTS

This work supported was by AFOSR under Grant No. FA9550-18-1-0066 and NSF under Grant No. DMR-18-00130. This work was also supported by AFOSR under Grant No. FA9550-18-1-0529 and made use of the Cornell Center for Materials Research Facilities supported by the NSF MRSEC program (No. DMR-1719875), and the Cornell NanoScale Science and Technology Facility, an NNCI member supported by NSF under Grant No. NNCI-2025233.

AUTHOR DECLARATIONS

Conflict of Interests

The authors have no conflicts to disclose.

Author Contributions

Micah S. Haseman: Data curation (lead); Formal analysis (lead); Visualization (lead); Writing – original draft (lead); Writing – review & editing (lead). **Daram N. Ramdin:** Formal analysis (equal); Software (lead). **Wenshen Li:** Formal analysis (equal); Resources (equal); Software (equal); Visualization (equal). **Kazuki Nomoto:** Resources (equal); Visualization (equal). **Debdeep Jena:** Conceptualization (supporting); Funding acquisition (equal); Resources (equal). **Huili Grace Xing:** Conceptualization (equal); Funding acquisition (equal); Methodology (equal); Resources (equal); Supervision (supporting); Writing – review & editing (supporting). **Leonard J. Brillson:** Conceptualization (lead); Funding acquisition (lead); Methodology (equal); Project administration (lead); Supervision (lead); Writing – original draft (supporting); Writing – review & editing (supporting).

DATA AVAILABILITY

The data that supports the findings of this study are available within the article and its supplementary material.

REFERENCES

[1]M. Higashiwaki, AAPPS Bull. **32**, 3 (2022).
[2]M. Higashiwaki and S. Fujita, in *Gallium Oxide: Materials Properties, Crystal Growth, and Devices* (Springer International Publishing, Cham, 2020).
[3]M. Higashiwaki, K. Sasaki, A. Kuramata, T. Masui, and S. Yamakoshi, Appl. Phys. Lett. **100**, 013504 (2012).
[4]G. H. Jessen, IEEE Spectr. **58**, 36 (2021).
[5]M. A. Mastro, A. Kuramata, J. Calkins, J. Kim, F. Ren, and S. J. Pearton, ECS J. Solid State Sci. Technol. **6**, P356 (2017).
[6]Z. Hu, K. Nomoto, W. Li, Z. Zhang, N. Tanen, Q. T. Thieu, K. Sasaki, A. Kuramata, T. Nakamura, D. Jena, and H. G. Xing, Appl. Phys. Lett. **113**, 122103 (2018).
[7]W. Li, Z. Hu, K. Nomoto, Z. Zhang, J.-Y. Hsu, Q. T. Thieu, K. Sasaki, A. Kuramata, D. Jena, and H. G. Xing, Appl. Phys. Lett. **113**, 202101 (2018).
[8]W. Li, K. Nomoto, Z. Hu, T. Nakamura, D. Jena, and H. G. Xing, in *2019 IEEE International Electron Devices Meeting IEDM* (IEEE, San Francisco, CA, 2019), pp. 12.4.1–12.4.4.
[9]W. Li, K. Nomoto, Z. Hu, D. Jena, and H. G. Xing, IEEE Electron Device Lett. **41**, 107 (2020).
[10]W. Li, D. Saraswat, Y. Long, K. Nomoto, D. Jena, and H. G. Xing, Appl. Phys. Lett. **116**, 192101 (2020).
[11]T. Moule, S. Dalcanale, A. S. Kumar, M. J. Uren, W. Li, K. Nomoto, D. Jena, H. G. Xing, and M. Kuball, IEEE Trans. Electron Devices **69**, 75 (2022).
[12]W. Li, K. Nomoto, Z. Hu, D. Jena, and H. G. Xing, IEEE Trans. Electron Devices **67**, 3938 (2020).
[13]W. Li, K. Nomoto, Z. Hu, D. Jena, and H. G. Xing, IEEE Trans. Electron Devices **68**, 2420 (2021).
[14]A. W. Ludikhuize, in *12th International Symposium on Power Semiconductor Devices ICs Proc. Cat No00CH37094* (IEEE, Toulouse, 2000), pp. 11–18.
[15]J. Sonsky and A. Heringa, in *IEEE International Devices Meeting 2005. IEDM Technical Digest* (IEEE, Tempe, 2005), pp. 373–376.
[16]M. Xian, R. Elhassani, C. Fares, F. Ren, M. Tadjer, and S. J. Pearton, J. Vac. Sci. Technol. B **37**, 061205 (2019).
[17]J. Yang, Z. Sparks, F. Ren, S. J. Pearton, and M. Tadjer, J. Vac. Sci. Technol. B **36**, 061201 (2018).
[18]J. L. Lyons, A. Janotti, and C. G. Van de Walle, J. Appl. Phys. **115**, 012014 (2014).
[19]T. Gake, Y. Kumagai, and F. Oba, Phys. Rev. Mater. **3**, 044603 (2019).
[20]J. B. Varley, A. Janotti, C. Franchini, and C. G. Van de Walle, Phys. Rev. B **85**, 081109 (2012).
[21]S. Marcinkevičius and J. S. Speck, Appl. Phys. Lett. **116**, 132101 (2020).
[22]Y. K. Frodason, K. M. Johansen, L. Vines, and J. B. Varley, J. Appl. Phys. **127**, 075701 (2020).
[23]P. Deák, Q. Duy Ho, F. Seemann, B. Aradi, M. Lorke, and T. Frauenheim, Phys. Rev. B **95**, 075208 (2017).
[24]Q. D. Ho, T. Frauenheim, and P. Deák, Phys. Rev. B **97**, 115163 (2018).
[25]B. E. Kananen, N. C. Giles, L. E. Halliburton, G. K. Foundos, K. B. Chang, and K. T. Stevens, J. Appl. Phys. **122**, 215703 (2017).
[26]Y. Wang, P. T. Dickens, J. B. Varley, X. Ni, E. Lotubai, S. Sprawls, F. Liu, V. Lordi, S. Krishnamoorthy, S. Blair, K. G. Lynn, M. Scarpulla, and B. Sensale-Rodriguez, Sci. Rep. **8**, 18075 (2018).
[27]S. Yamaoka and M. Nakayama, Phys. Status Solidi C **13**, 93 (2016).
[28]S. Modak, L. Chernyak, A. Schulte, M. Xian, F. Ren, S. J. Pearton, A. Ruzin, S. S. Kosolobov, and V. P. Drachev, AIP Adv. **11**, 125014 (2021).
[29]T. Onuma, S. Fujioka, T. Yamaguchi, M. Higashiwaki, K. Sasaki, T. Masui, and T. Honda, Appl. Phys. Lett. **103**, 041910 (2013).
[30]A. Kyrtsos, M. Matsubara, and E. Bellotti, Phys. Rev. B **95**, 245202 (2017).
[31]M. A. Blanco, M. B. Sahariah, H. Jiang, A. Costales, and R. Pandey, Phys. Rev. B **72**, 184103 (2005).
[32]H. Gao, S. Muralidharan, M. R. Karim, S. M. White, L. R. Cao, K. Leedy, H. Zhao, D. C. Look, and L. J. Brillson, J. Phys. Appl. Phys. **53**, 465102 (2020).
[33]H. Gao, S. Muralidharan, N. Pronin, M. R. Karim, S. M. White, T. Asel, G. Foster, S. Krishnamoorthy, S. Rajan, L. R. Cao, M. Higashiwaki, H. von Wenckstern, M. Grundmann, H. Zhao, D. C. Look, and L. J. Brillson, Appl. Phys. Lett. **112**, 242102 (2018).
[34]M. D. McCluskey, J. Appl. Phys. **127**, 101101 (2020).
[35]J. B. Varley, J. R. Weber, A. Janotti, and C. G. Van de Walle, Appl. Phys. Lett. **97**, 142106 (2010).
[36]L. Dong, R. Jia, B. Xin, B. Peng, and Y. Zhang, Sci. Rep. **7**, 40160 (2017).
[37]Z. Zhang, E. Farzana, A. R. Arehart, and S. A. Ringel, Appl. Phys. Lett. **108**, 052105 (2016).
[38]E. Farzana, M. F. Chaiken, T. E. Blue, A. R. Arehart, and S. A. Ringel, APL Mater. **7**, 022502 (2019).
[39]C. Liu, Y. Berencén, J. Yang, Y. Wei, M. Wang, Y. Yuan, C. Xu, Y. Xie, X. Li, and S. Zhou, Semicond. Sci. Technol. **33**, 095022 (2018).
[40]Q. Shi, Q. Wang, D. Zhang, Q. Wang, S. Li, W. Wang, Q. Fan, and J. Zhang, J. Lumin. **206**, 53 (2019).
[41]J. Hao and M. Cocivera, J. Phys. Appl. Phys. **35**, 433 (2002).

[42]Y. Nie, S. Jiao, S. Li, H. Lu, S. Liu, S. Yang, D. Wang, S. Gao, J. Wang, and Y. Li, J. Alloys Compd. **900**, 163431 (2022).
[43]L. Binet and D. Gourier, J. Phys. Chem Solids **59**, 1241 (1998).
[44]T. Onuma, Y. Nakata, K. Sasaki, T. Masui, T. Yamaguchi, T. Honda, A. Kuramata, S. Yamakoshi, and M. Higashiwaki, J. Appl. Phys. **124**, 075103 (2018).
[45]S. Modak, L. Chernyak, A. Schulte, C. Sartel, V. Sallet, Y. Dumont, E. Chikoidze, X. Xia, F. Ren, S. J. Pearton, A. Ruzin, D. M. Zhigunov, S. S. Kosolobov, and V. P. Drachev, APL Mater. **10**, 031106 (2022).
[46]G. Pozina, M. Forsberg, M. A. Kaliteevski, and C. Hemmingsson, Sci. Rep. **7**, 42132 (2017).
[47]R. Lingaparthi, Q. T. Thieu, K. Sasaki, A. Takatsuka, F. Otsuka, S. Yamakoshi, and A. Kuramata, ECS J. Solid State Sci. Technol. **9**, 024004 (2020).
[48]J. Jesenovec, M. H. Weber, C. Pansegrau, M. D. McCluskey, K. G. Lynn, and J. S. McCloy, J. Appl. Phys. **129**, 245701 (2021).
[49]S. Mu, M. Wang, J. B. Varley, J. L. Lyons, D. Wickramaratne, and C. G. Van de Walle, Phys. Rev. B **105**, 155201 (2022).
[50]A. Janotti and C. G. Van de Walle, Nat. Mater. **6**, 44 (2007).
[51]J. B. Varley, H. Peelaers, A. Janotti, and C. G. Van de Walle, J. Phys.: Condens. Matter **23**, 334212 (2011).
[52]Y. Qin, M. Stavola, W. B. Fowler, P. Weiser, and S. J. Pearton, ECS J. Solid State Sci. Technol. **8**, Q3103 (2019).
[53]A. Y. Polyakov, N. B. Smirnov, I. V. Shchemerov, E. B. Yakimov, J. Yang, F. Ren, G. Yang, J. Kim, A. Kuramata, and S. J. Pearton, Appl. Phys. Lett. **112**, 032107 (2018).
[54]J. H. Leach, K. Udwary, J. Rumsey, G. Dodson, H. Splawn, and K. R. Evans, APL Mater. **7**, 022504 (2019).
[55]H. Murakami, K. Nomura, K. Goto, K. Sasaki, K. Kawara, Q. T. Thieu, R. Togashi, Y. Kumagai, M. Higashiwaki, A. Kuramata, S. Yamakoshi, B. Monemar, and A. Koukitu, Appl. Phys. Express **8**, 015503 (2015).
[56]M. Yamaga, T. Ishikawa, M. Yoshida, T. Hasegawa, E. G. Villora, and K. Shimamura, Phys. Status Solidi C **8**, 2621 (2011).
[57]X. Zhou, Y. Ma, G. Xu, Q. Liu, J. Liu, Q. He, X. Zhao, and S. Long, Appl. Phys. Lett. **121**, 223501 (2022).
[58]M. Yamaga, E. G. Víllora, K. Shimamura, N. Ichinose, and M. Honda, Phys. Rev. B **68**, 155207 (2003).
[59]W. Li, Z. Hu, K. Nomoto, R. Jinno, Z. Zhang, T. Q. Tu, K. Sasaki, A. Kuramata, D. Jena, and H. G. Xing, in *2018 IEEE International Electron Devices Meeting IEDM* (IEEE, San Francisco, CA, 2018), pp. 8.5.1–8.5.4.
[60]M. Zakria, D. J. Rogers, J. Scola, L. Zhu, M. Lockrey, P. Bove, E. V. Sandana, F. H. Teherani, M. R. Phillips, and C. Ton-That, Phys. Rev. Mater. **6**, 035202 (2022).
[61]N. H. Nickel and K. Geilert, Appl. Phys. Lett. **116**, 242102 (2020).
[62]S. Kumar, T. Kamimura, C.-H. Lin, Y. Nakata, and M. Higashiwaki, Appl. Phys. Lett. **117**, 193502 (2020).
[63]W. Li, K. Nomoto, Z. Hu, D. Jena, and H. G. Xing, Appl. Phys. Express **12**, 061007 (2019).
[64]B. Chatterjee, W. Li, K. Nomoto, H. G. Xing, and S. Choi, Appl. Phys. Lett. **119**, 103502 (2021).